AIAA JOURNAL
Vol. 50, No. 7, July 2012

Passive Control of High-Speed Separated Flows Using Splitter Plates

Todd M. Reedy,* Gregory S. Elliott,† and J. Craig Dutton‡
University of Illinois at Urbana–Champaign, Urbana, Illinois 61801
and
Yeol Lee§
Korea Aerospace University, Goyang 412-791, Republic of Korea

DOI: 10.2514/1.J051566

An experimental investigation was conducted to study the effects of passive splitter plates placed in the recirculation region behind a blunt-based axisymmetric body aligned in supersonic flow (Mach 2.49). The goals of this research were to obtain a better understanding of the physical phenomena that govern these massively separated high-speed flows and to determine the flow-control authority of these passive devices. Triangular splitter plates dividing the near wake into one-half-, one-third-, and one-fourth-cylindrical regions were designed to exploit specific stability characteristics of this flow, to affect the near-wake flow, to alter the base pressure, and to ultimately affect base drag. Mean and high-frequency static-pressure measurements were acquired on the base to assess the influence of these plates. Schlieren imaging, surface flow visualization, and pressure-sensitive paint measurements were also employed to document the near-wake flowfield, surface flow structure, and surface pressure, respectively. The time-averaged base pressure distribution, time-series pressure fluctuations, and presumably the stability characteristics were altered by the spatial division of the near wake. The area-integrated pressure was only slightly affected. Normalized root-mean-square levels indicate pressure fluctuations were significantly reduced (as much as 39%) with the addition of the splitter plates. Power-spectral-density estimates revealed a spectral broadening of fluctuating energy for the one-half-cylinder configuration and a bimodal distribution for the one-third- and one-fourth-cylinder configurations.

Nomenclature

base	=	base condition
C_{Dnet}	=	coefficient of drag, net
f	=	frequency
$G_{pp}(f)$	=	one-sided power spectral density
l	=	distance along splitter plate diagonal edge
L_{edge}	=	length of splitter plate diagonal edge
L_{SP}	=	length of splitter plate along centerline
P	=	static pressure
r	=	radial coordinate
R_0	=	base radius
x	=	axial coordinate
∞	=	freestream condition

I. Introduction

HIGH-SPEED separated flows are not fully understood despite a considerable body of work. These flows are difficult to predict accurately due to complex fluid dynamic phenomena, including the presence of shock waves, expansion waves, large flow property gradients, recirculating flow regions, large Reynolds numbers, and turbulent, highly compressible shear layers. Understanding the fluid dynamic mechanisms in the near-field region behind bodies of revolution is crucially important for predicting high-speed projectile and flight vehicle performance. Specifically, the low pressure acting on the rear-facing base of cylindrical blunt bodies in supersonic flight can cause significant amounts of aerodynamic drag [1].

Figure 1 is a schematic of the *time-mean* near-wake flow structure that occurs aft of a cylindrical afterbody aligned with supersonic flow. The turbulent boundary layer of the supersonic afterbody flow separates at the base corner where a strong expansion is centered. The resulting free shear layer that develops after separation is a key component contributing to the near-wake flow. It divides the high-speed outer inviscid flow from the lower-speed recirculation region, and it is highly turbulent [2] and compressible [3]. As the shear layer approaches the axis of symmetry of the afterbody, a recompression process occurs as the flow realigns itself with the axial freestream flow direction. The entrainment characteristics of the shear layer essentially set the base pressure by determining the fraction of shear layer fluid that is unable to negotiate the adverse pressure gradient imposed by the recompression waves near the rear stagnation point and is therefore returned toward the base. The recirculation region has been found to be quite energetic with velocities up to approximately 150 m/s and Mach numbers up to about 0.5 in typical applications [2]. Therefore, the inner edge of the shear layer is bounded by a dynamic, turbulent, subsonic recirculating flow and is not the "dead-air" region envisioned in the original component models of this flow [4,5].

It should be emphasized that the schematic presented in Fig. 1 is a highly simplified time-averaged representation of the separated flow. In reality, these high-speed base flows are unsteady and on an instantaneous basis are composed of dominant large-scale turbulent structures [6] with significant flapping and convolution of the shear layer and trailing wake [7]. It has been shown that large turbulent structures dominate this flow, particularly in the latter stages of the free shear layer and in the recompression and reattachment regions near the rear stagnation point. Controlling these large structures and the instability mechanisms that generate them is an important objective of the present work as this has the potential for controlling

Presented as Paper 2011-0484 at the 49th AIAA Aerospace Sciences Meeting, Orlando, FL, 4–7 January 2011; received 19 August 2011; revision received 24 February 2012; accepted for publication 9 March 2012.

*Graduate Research Assistant, Mechanical Science and Engineering, 1206 West Green Street. Student Member AIAA.
†Professor and Associate Head, Aerospace Engineering, 104 South Wright Street. Associate Fellow AIAA.
‡Bliss Professor, Aerospace Engineering, 104 South Wright Street. Associate Fellow AIAA.
§Professor, School of Aerospace and Mechanical Engineering. Member AIAA.

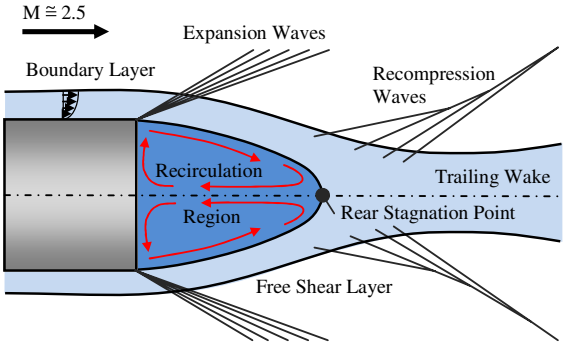

Fig. 1 Schematic of mean near-wake flowfield for blunt cylindrical afterbody.

the mass entrainment from the recirculation region into the shear layer and thus the base pressure.

Numerical simulations of these high-speed separated flows have been performed for the last 30 or so years. Reynolds-averaged Navier—Stokes (RANS) simulations [8–10] have been shown to predict mean base pressure and some basic flow features reasonably well; however, they have proved unsuccessful for predicting base pressure distributions and fundamentally important quantities, including shear layer growth rate and turbulent stresses. Large-eddy simulation (LES) [11] has been reasonably successful but can still be too computationally expensive for separated base flows with realistic Reynolds numbers due to the fine mesh resolution requirements especially near the afterbody and base surfaces. Substantial work has also been performed to combine the advantages of RANS and LES into methods called detached eddy simulations, zonal-detached eddy simulation, and flow simulation methodology, to better tackle the base flow challenge [12–16]. These hybrid computations have shown encouraging agreement with previous base pressure and flowfield measurements. Simon et al. [14] successfully probed, in an instantaneous sense, the compressible mixing layer and recirculation region to capture characteristic frequencies of the flow. Sivasubramanian et al. [15] have numerically demonstrated altered near-wake and base pressure quantities by introducing perturbations to simulate passive and active flow control. Weiss and Deck [16] analyzed the influence of continuous jets on an axisymmetric step to control the antisymmetric azimuthal instability mode.

Passive and active flow controls are popular areas of current fluid dynamics research. Active flow-control techniques such as mechanical flaps [17], mass injection [18], and plasma actuators [19] have been shown to influence external flows. However, these methods can possess limitations in supersonic applications and require additional energy input. Passive technologies, specific to bodies of revolution in supersonic flows, such as boattailing [20,21] or base bleed [9,22] have proved to increase base pressure and reduce drag with no such energy addition. Obviously, discovering additional passive flow-control methods that could be implemented within the regimes of interest with similar benefits would prove advantageous to the flight of projectiles and other separated flows.

Recent direct numerical simulation (DNS) results [23–25] have shown that physically altering the near-wake region could potentially yield a change in base pressure, alter base drag, and increase flight vehicle performance. Specifically, Sandberg and Fasel [23] conducted DNS of various computational domain sizes aft of a cylindrical afterbody to highlight large-scale coherent structures. By deliberately eliminating certain low-order azimuthal instability modes, mean base pressure was shown to increase for an axisymmetric body submerged in a $M = 2.5$ flow at $Re_D = 3(10^4) - 1(10^5)$ [24]. The appropriate experimental analog to eliminating these low-order modes is to include physical splitter plates (SPs) to divide the near wake into segments. This is the approach that has been used in the current experimental study.

Accordingly, an experimental investigation of the base pressure and near-wake flowfield downstream of a blunt-based axisymmetric body in supersonic flow has been conducted to better understand the physical phenomena that govern these massively separated high-speed flows. Passive flow-control experiments were performed by inserting triangular SPs into the recirculation region behind the cylindrical base to alter the stability characteristics and flow structure of the near-wake flowfield. Dividing the near wake into one-half-, one-third-, and one-fourth-cylindrical regions, the goal of these plates was to eliminate the dominant low-order azimuthal instability modes in the recirculation region, affect the near-wake flow and reattachment length, and ultimately alter the base pressure as suggested by the previous DNS work of Sandberg and Fasel [24].

II. Experimental Setup

An axisymmetric, open-jet, supersonic, blowdown-type wind tunnel with a centered cylindrical sting was reconstructed specifically for these base flow experimental studies. Figure 2 is a schematic of the nominally Mach 2.5 tunnel that is located in Aeronautical Laboratory A at the University of Illinois at Urbana–Champaign. Once operated in the Mechanical Engineering Laboratory, components of the pre-existing tunnel were refurbished and assembled with a newly designed inlet, diffuser, and exhaust system.

Dry, filtered compressed air was supplied at 34 m^3/min and 1 MPa by an Ingersoll-Rand compressor to a 140 m^3 tank farm. Airflow from the supply tanks to the stagnation chamber was controlled by a Valtek Mark I pneumatic control valve. Integrated with a proportional-integral-derivative control algorithm, the control valve continuously throttles the flow to maintain the desired stagnation pressure. Depending on the passive control device installed, the operating stagnation pressure ranged between 380 to 400 ± 1.9 kPa for the current experiments, which resulted in a tunnel run time of approximately 100 s. After passing through a flow conditioning module (screen and honeycomb), the air was accelerated by an annular converging—diverging nozzle. Upon exiting the nozzle (14.4 cm exit diameter), the supersonic stream entered the 25.4-cm-diam by 30.5-cm-long test section, which contained three fused silica windows for optical access to the flow. A converging cylindrical flow catcher, constant-area cylindrical supersonic diffuser, and conically divergent subsonic diffuser decelerated the flow before being silenced by perforated duct and an exhaust muffler and exiting to the atmosphere.

Tunnel operating pressures were determined by matching the pressure at the nozzle exit to that of the outer separated zone (test section region). By matching these pressures, potential interference waves emanating from the nozzle exit lip were eliminated. The mean Mach number and unit Reynolds number of the freestream flow at the nozzle exit were 2.49 and 40 (10^6) per meter, respectively. The thickness of the boundary layer approaching the base corner separation point was estimated from previous measurements [2] to be 3.2 mm.

The test model arrangement was composed of three components: 1) the stainless steel sting, 2) the common cylindrical afterbody model, and 3) the SP configuration as shown in Fig. 3. A 63.5-mm-

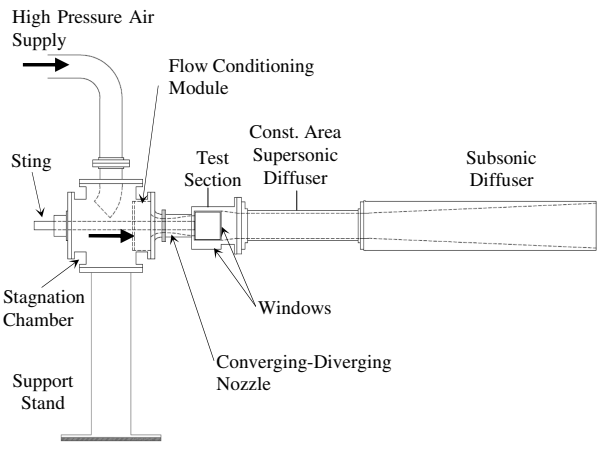

Fig. 2 Schematic of axisymmetric wind tunnel.

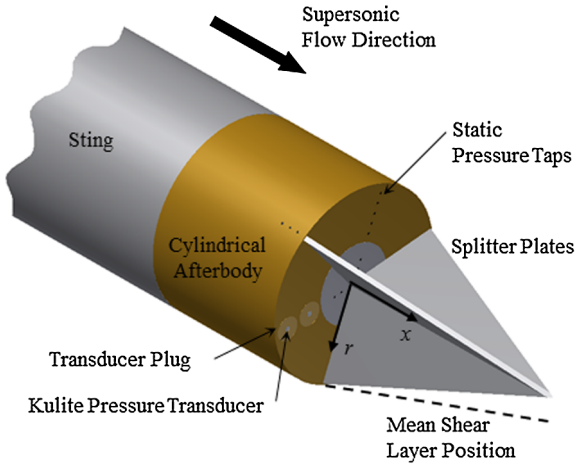

Fig. 3 Schematic of afterbody/base model and SPs.

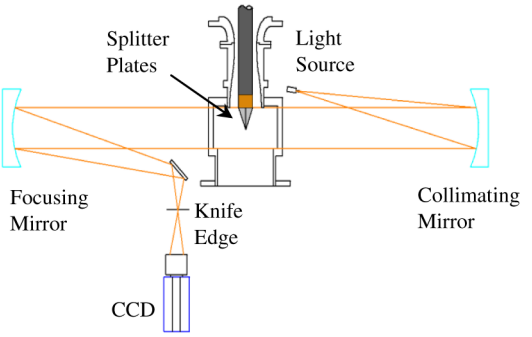

Fig. 5 Schematic of schlieren imaging technique.

diam cylindrical sting ran through the stagnation chamber and was physically supported upstream of the nozzle to prevent any interference waves from supports in the near-wake region of the flow. Attached to the downstream end of the sting by internal threads, the base model terminated at the exit plane of the nozzle. The afterbody/base model is interchangeable to accommodate investigations of different flow-control schemes, including the SP configurations described herein. The SPs were welded to plugs that were securely fastened and sealed to the cylindrical afterbody. The joints of the SPs were sealed with epoxy.

Four configurations were tested, as shown in Fig. 4: a no-flow-control (flat-base) geometry used as a baseline for comparison and three SP arrangements dividing the cylindrical base into one-half-, one-third-, and one-fourth-cylindrical regions. Each of the SP configurations was constructed of 1.6-mm-thick stainless steel, tapered, triangular SP(s) that were submerged only in the recirculating region behind the base model. The centerline length of the SP, L_{SP}, was set to match the rear stagnation point (or reattachment point) distance measured previously by Herrin and Dutton [2] for the no-control case; this distance was $x/R_0 = 2.65$, which corresponds to a length of 84.1 mm for the current afterbody model. The mean reattachment length has been noted as an important scaling parameter for separated flows [26]. The design of these SPs was such to eliminate the low-order azimuthal instability modes exclusively within the recirculation region. In this way, the plates were not immersed in any portion of the high-speed shear layer or supersonic freestream, which could contribute to large viscous and/or shock wave effects.

III. Experimental Diagnostics

Schlieren imaging from the conventional z-type configuration, shown in Fig. 5, was used to qualitatively investigate the near-wake flowfield for the various SP models. Schlieren photographs were also used in determining the proper operating condition that eliminated interference waves from the tunnel in the near-field region of interest. The optical setup used a Thorlabs light-emitting diode (LED) (model MWLED) as the light source, a pair of 20.3-cm-diam parabolic mirrors with a focal length of 1.6 m, a small, square flat mirror, and a horizontal knife edge. A high-resolution unintensified Cooke PCO.1600 charge-coupled device (CCD) camera with a *C*-mounted Nikon Nikkor lens was used to collect the schlieren images.

Surface flow visualization was conducted on the rear-facing base and on the SP surfaces to investigate the surface flow patterns and large-scale flow structure within the recirculation region. The medium used was a combination of titanium dioxide, silicone oil, and oleic acid. Flow visualization images during tunnel startup and steady-state flow conditions were captured with a Mightex buffered CCD camera. Steady-state images were analyzed with an image processing algorithm (based on image intensities) to detect the average location of a separation ring observed on the base surface for each configuration. For each case, more than 100 images were analyzed to compute the separation ring radial locations, which were found to be repeatable between trials.

The main focus of this investigation involved documenting pressure on the rear-facing base using mean static-pressure measurements via taps, pressure-sensitive paint (PSP) measurements, and high-frequency pressure measurements. The purpose of these measurements was to examine whether subdivision of the wake and the consequent elimination of the low-order azimuthal instability modes in the recirculation region yield an altered base pressure distribution. Mean static-pressure measurements were obtained using radially distributed taps on the base connected to Pressure Systems, Inc. pressure scanners (Netscanner model 98RK and modules Model 9816). There were two arrays of static taps, separated by 120 deg, each with seven pressure taps (0.79 mm in diameter) located across the radius of the base. Taps were located radially at 4.9, 7.7, 15.8, 19.0, 22.2, 25.4, and 28.6 mm (corresponding to $r/R_0 = 0.154$, 0.242, 0.5, 0.6, 0.7, 0.8, and 0.9) from the center. Along the afterbody, there were two sets of three taps, located at 3.2, 6.4, and 9.6 mm axially upstream of the base corner. In all cases, tubing from the model pressure taps to the transducers was routed through the hollow sting. For each case, the SP configurations were arranged such that at least one radial array of taps was located down the middle of the divided region. Additionally, the wind tunnel is equipped with total pressure and temperature probes mounted in the stagnation chamber, four static-pressure taps circumferentially spaced around the nozzle exit, and four static-pressure taps circumferentially spaced on the upstream wall in the test section.

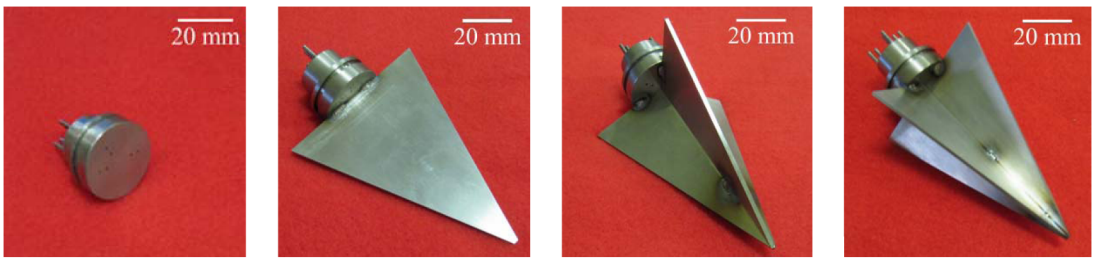

a) b) c) d)

Fig. 4 Splitter plate configurations: a) no-control, b) one-half cylinder, c) one-third cylinder, and d) one-fourth cylinder.

Static-pressure measurements were acquired with 0–103 kPa differential transducers with ±0.05% full-scale accuracy, whereas stagnation pressure was acquired with a 0–690 kPa differential transducer with ±0.05% full-scale accuracy. The reference ports of the differential transducers were exposed to atmospheric pressure, which was recorded for each test by a Pressure Systems, Inc. Model 9034 pressure calibrator capable of measuring 0–310 kPa with 0.01% full-scale accuracy. Extensive care was taken to ensure that the axes of the sting and annular nozzle were coincident; however, this alignment accuracy was the largest contributor to pressure uncertainty. A complete error analysis was conducted to estimate the *worst-case* uncertainty of 2.9% in the base pressure ratio and 3.3% in drag coefficient.

Employing PSP yielded spatially continuous surface pressure measurements on the model base and SPs. This allowed for a more complete documentation of the pressure distribution including radial and azimuthal gradients along the base and plates. Figure 6 shows a schematic of the PSP setup. A single probe luminescent paint (ISSI UNIFIB-400) was excited using pulsed light from a blue LED array (model ISSI LM2-470). A bandpass filter was placed on the lamp so that the incident light in the range of the luminescent signal wavelength was mostly filtered. The luminescent signal from the painted surfaces was then filtered using a 610 nm high-pass filter to eliminate the excitation light. Averaged, intensity images of 80 ms exposure were captured using a Cooke PCO.1600 CCD camera and were digitally stored for later processing. In situ calibrations were performed using the static-pressure taps on the base. For the SP calibrations, several trials were conducted at slightly different stagnation pressures (and base pressures) to account for the span the pressures experienced by the plates. Calibration curves used a linear fit and had coefficients of determination of $R^2 = 0.958$ for the no-control case and at least $R^2 = 0.991$ for the SP configurations. Based on the uncertainty in the calibration curves and aforementioned static base pressure measurements, the maximum uncertainty in the PSP measurements normalized by the freestream pressure was approximately ±0.03.

High-frequency pressure measurements were made with a Kulite transducer. A single Kulite XCS-062 pressure transducer, with a sensor diameter of 0.71 mm and pressure range of 0–68.59 kPa, was rigidly mounted into a brass plug with room temperature vulcanized rubber. The axis of the transducer was aligned along the centerline of the plug with the transducer screen flush with the outer face of the plug. High-frequency pressure measurements were obtained at radial locations of 17.8 and 26.7 mm (corresponding to $r/R_0 = 0.56$ and 0.84) from the base center. Similar to the static taps, the high-frequency transducers were located down the middle of the divided region for the SP configurations. The Kulite transducer used was quoted to have a combined nonlinearity, hysteresis, and repeatability, that is, a measurement uncertainty, of 0.1% of full scale. The transducer was statically calibrated in situ for each location and SP combination using the Pressure Systems, Inc. Model 9034 pressure calibrator. As demonstrated by previous authors, static calibration of these transducers is accurate to within a few percent of the dynamic value [27]. The transducer was powered by a Vishay Model 2311 signal conditioning amplifier with a nominal excitation of 10 V dc Time-series data output from the transducer was amplified before being filtered through a Krohn-Hite Model 3342 filter with a cutoff frequency of 50 kHz. The filtered signal was then passed through a National Instruments BNC-2110 connector block and a 16-bit National Instruments PCI-6120 A/D data acquisition card. A LabVIEW program acquired time-history records of 83,334 samples at a sampling frequency of 166,668 Hz. Power-spectral-density (PSD) estimates were calculated using the built-in LabVIEW PSD analysis block. Sixty-four records of 0.5 s length were analyzed with linear weighting for each dataset. A Hanning window was used to suppress side-lobe leakage. The PSD estimates had a frequency resolution of 2 Hz.

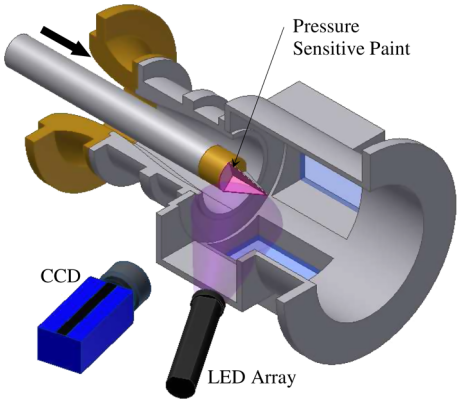

Fig. 6 Schematic of PSP technique.

IV. Results and Discussion

A comparison of the aforementioned experimental diagnostics for the four cases will now be presented. In all images presented, the flow direction is left to right. Schlieren images were obtained perpendicular to the freestream flow, whereas the surface flow visualization and PSP images were obtained at an off-axis angle to the base. Unless otherwise noted, these images were not geometrically transformed.

A. Flow Visualizations

No-control experiments were conducted with the flat-base configuration to validate the flowfield in the axisymmetric wind-tunnel facility and to act as baseline data. Schlieren images of the flat-based model, shown in Fig. 7a, confirmed the supersonic nature and lack of interference waves in the near-field region of interest. The shear layer from the test section sudden expansion is clearly seen as the upper dark horizontal streak and the lower light streak in each image. The dominant flow structures expected in the near wake are clearly present, including the axially converging shear layer separating the high-speed freestream fluid from the slower recirculation fluid, the expansion fans emanating from the base corners, the recompression waves as fluid navigates the adverse pressure gradient near the rear stagnation point, and finally the closed, developing wake. Schlieren images for the one-half-, one-third-, and one-fourth-cylinder SP configuration experiments are shown in Figs. 7b–7d, respectively, and reveal similar key flow structures. For each arrangement, the mean shear layer shape remains relatively unchanged, and the separated near-wake merges downstream of the SP tip.

Surface flow visualization on the no-control base confirms the axially symmetric nature of the flow by producing radially outward streaklines during tunnel startup as shown in the left image in Fig. 8a. At steady-state operating conditions, a separation ring, shown in the right image in Fig. 8a as a distinct ring of the accumulated flow visualization medium, was observed at approximately $r/R_0 = 0.85 \pm 0.04$, where the radially outward recirculating flow along the base meets the shear layer influence. Shown in Figs. 8b–8d, surface flow visualizations for the different SP cases at steady-state operation were all comparable in structure. Similar to the no-control case, streaklines on the base were generally radially outward. The average locations of the separation rings on the base surface were observed near $r/R_0 = 0.84 \pm 0.03$, 0.82 ± 0.03, and 0.83 ± 0.02 for the one-half-, one-third-, and one-fourth-cylindrical cases, respectively, where flow separated from the base and turned downstream.

In all cases, surface flow visualization medium at the downstream tip of the SP(s) traversed upstream, indicating the existence of large-scale recirculation. No interaction of the shear layer on the diagonal edges of the SPs was observed. A separation line formed near $x/L_{SP} = 0.10$ where the reversed flow on all of the plates turned away from the axis of symmetry. Upstream of this separation line, flow moved downstream and outward. In these small regions along the perpendicular joints where the SPs join with the base, streaklines suggested a helical vortex structure flowing radially outward, possibly associated with secondary recirculation regions. Secondary

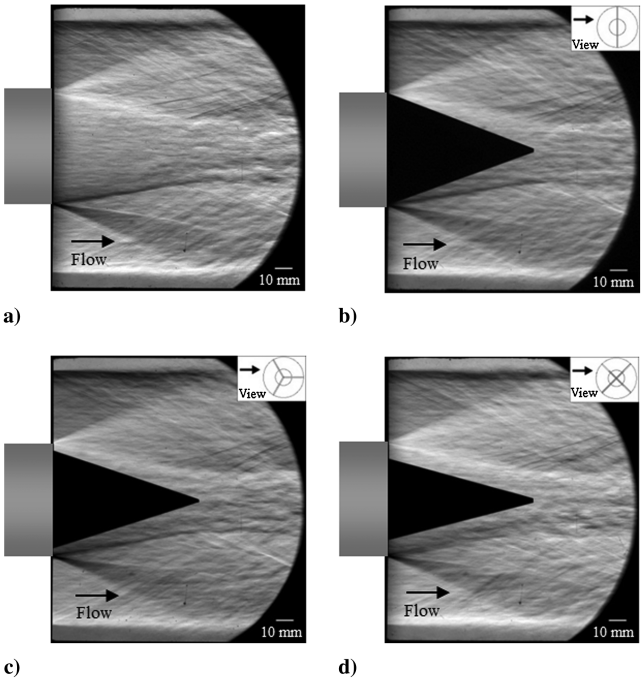

Fig. 7 Instantaneous schlieren images: a) no control, b) one-half-cylinder SP, c) one-third-cylinder SP, and d) one-fourth-cylinder SP.

recirculation regions have been previously evidenced in corners [28–30] but have not been thoroughly investigated, especially for axisymmetric geometries. Hall et al. [28] used particle image velocimetry to reveal a highly three-dimensional secondary corner vortex for a backward-facing step geometry. Additionally, they reported a secondary vortex separation point (i.e., the interface between the primary and secondary vortex) normalized by the shear layer separation length equal to 0.11, which compares well with the current experiment.

B. Mean Pressure Measurements

Mean static pressures along the base for the no-control and various SP arrangements were measured and are presented, normalized by the average freestream static pressure, in Fig. 9. Time-averaged pressure measurements from the high-frequency transducers are also included. The bars (some of which are smaller than the data symbols) are representative of plus or minus one standard deviation in the collected data. Base pressure measurements for the no-control case matched previous results [2], indicating a nearly constant pressure across the base with only a slight increase with increasing radius. Dividing the near-wake region with the SPs clearly altered the base pressure radial distribution. Unlike the baseline case, the highest pressures for the SP cases were recorded near the center, in all cases higher than the no-control case. However, the outer taps measured lower pressures than for no control. These trends are in line with the DNS results with reduced azimuthal domains sizes [24] and consistent with the elimination of low-order modes (long wavelengths) that are responsible for a constant pressure distribution

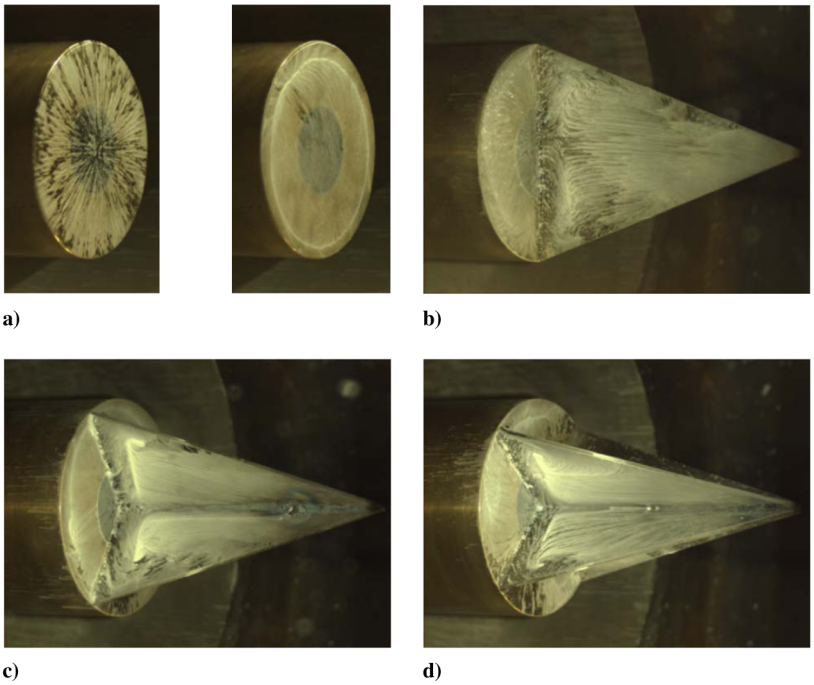

Fig. 8 Instantaneous surface flow visualizations: a) no control during startup (left) and steady state (right), b) one-half-cylinder SP, c) one-third-cylinder SP, and d) one-fourth-cylinder SP.

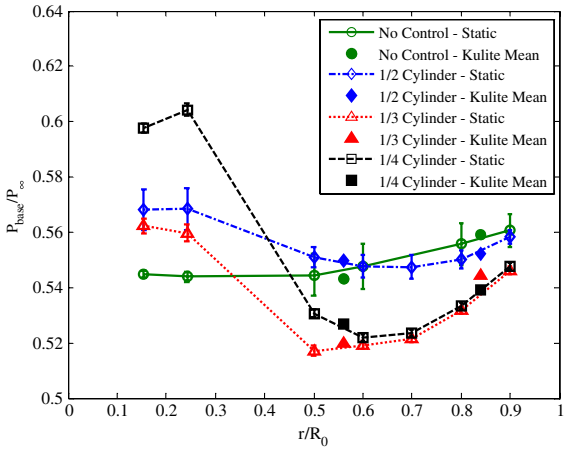

Fig. 9 Base pressure distribution.

on the base. Integrating the base pressure distribution for the no-control configuration yielded a net base drag coefficient of $C_{\text{Dnet}} = 0.1028$ (in good agreement with the previously reported C_{Dnet} of 0.102 [2]). For the one-half-, one-third-, and one-fourth-cylinder SP configurations, the resulting net base drag coefficients were $C_{\text{Dnet}} = 0.1033$, 0.1071, and 0.1051, respectively. Comparing against the no-control geometry, the SPs produced changes in drag coefficient of +0.5, +4.2, and 2.2%, which are within or very close to the uncertainty of the measurements.

Despite altering the base pressure distribution to exhibit a more distinct radial variation, the insertion of the dividing SPs did not lead to a net base drag reduction as suggested in certain cases examined in previous DNSs [24]. Several differences between the experiments and simulations could contribute to the differences in these results. In the simulations, the flow was transitional, i.e, significantly lower Reynolds number based on the cylinder diameter of $Re_D = 3(10^4) - 1(10^5)$ compared to that of the fully turbulent experimental Reynolds number of $Re_D = 2.5(10^6)$. Additionally, the physical SPs are conjectured to only eliminate the azimuthal instability modes in the recirculation region, not the shear layer. This highlights the significance of instabilities and turbulent structures contained in the shear layer and their influence on the base pressure. Furthermore, the SPs provide tangible, solid surfaces (with finite volume and viscous effects) for the downstream shear layer to reattach to, which is known to influence the reattachment process [30,31].

Pressure-sensitive paint measurements on the base and on the SPs were also acquired. Presented in Fig. 10a, PSP measurements confirmed the nearly constant pressure distribution for the no-control case. For this case only, the PSP image was geometrically transformed to provide a true end-view perspective. Spatial distributions of pressure from PSP measurements for the one-half-, one-third-, and one-fourth-cylindrical SP configurations are shown in Figs. 10b–10d, respectively. Comparisons between the static tap pressure measurements and base PSP measurement profiles for each of the SP configurations indicated consistent agreement to within the estimated uncertainties of the two measurement techniques. On the base surfaces, an extremely small azimuthal dependence was observed for each of the configurations. On the SP surfaces, the pressure distribution in the axial direction is qualitatively similar for all cases. Closest to the base, the SPs experience a comparable pressure to that acting on the base, corresponding to the low pressure following the expansion fan. Progressing downstream along the plate, the pressure decreases before recompressing. The pressure recovers nearly to the freestream pressure by the tip of the SPs. Slight discrepancies between pressure measurements on adjacent plates in the one-third- and one-fourth-cylinder arrangements can be attributed to the uncertainty in the axial alignment of the model and nozzle as well as the uncertainty of the measurement technique itself. Pressure anomalies at the SP joints were not physical as they were a result of an undesirable interaction between the luminescent paint and the epoxy used to seal the joints.

Figures 11a and 11b shows pressure traces extracted from the PSP data along the centerlines of the SPs in the axial direction and along the top diagonal edges, respectively. In Fig. 11a, the axial distance is normalized by the length of the SP, whereas in Fig. 11b the diagonal distance along the SP edge is normalized by the total diagonal length. Because the epoxy along the SP joints for the one-third- and one-fourth-cylinder cases, accurate centerline traces were not possible and so traces directly above the joint representative of the centerline are shown. It is shown that the insertion of the SPs alters the pressure in the recirculating region, which was previously suggested to be constant by Amatucci et al [32]. All of the centerline traces are qualitatively similar in nature, but as the number of subdivisions is increased, a general increase in pressure was observed. For the one-half-cylinder case, the pressure trace was well behaved with a small decrease in pressure away from the base then a steady recompression

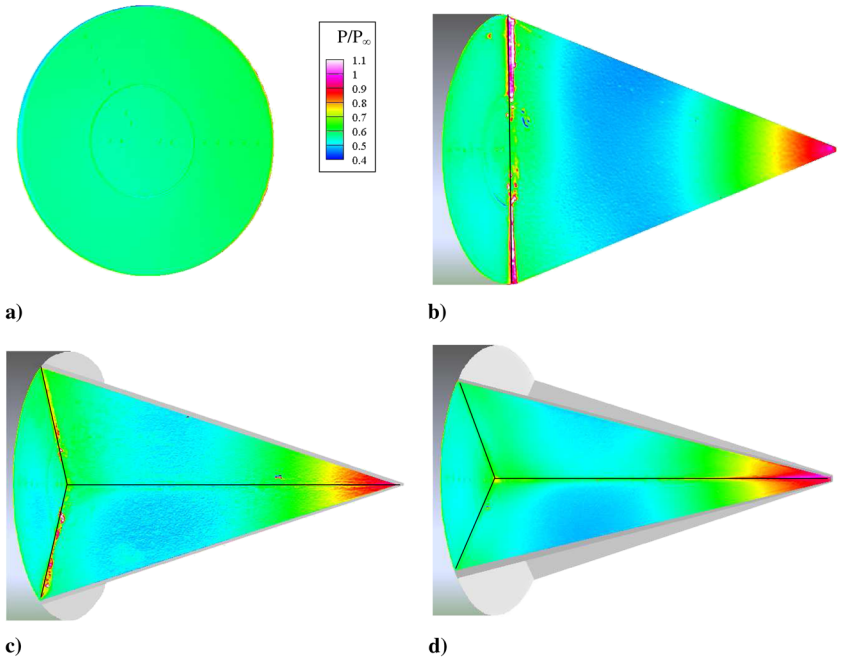

Fig. 10 PSP pressure distributions: a) no-control, b) one-half-cylinder SP, c) one-third-cylinder SP, and d) one-fourth-cylinder SP.

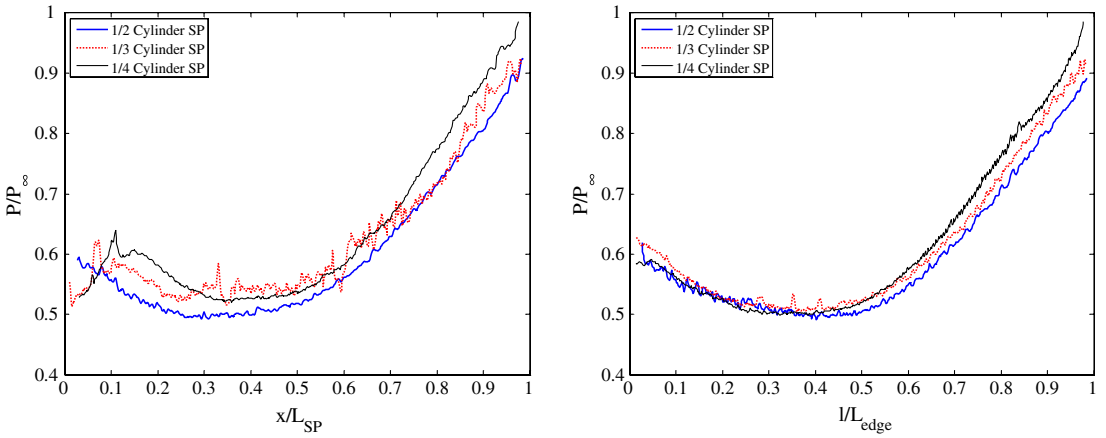

Fig. 11 PSP pressure traces along the SP a) centerline and b) top diagonal edge.

through to the SP tip. For the one-third- and one-fourth-cylinder cases, a noticeable interaction near the base was present. A local pressure peak is observed near the base and is shown to grow in magnitude and move downstream as the number of subdivisions increases. It is thought that these peaks are attributable to the interaction of the large-scale recirculation along the plate and the smaller helical bubble in the corner where the SP meets the base. Further downstream along the plates, the beginning of the adverse pressure gradient associated with flow reattachment was approximated near $x/L_{\mathrm{SP}} = 0.5$.

For the outer diagonal edge plot in Fig. 11b, the pressure traces are more similar among the different cases than for the centerline plots. Near to the base where the plate edges are farthest apart, the traces collapse. There is a slight difference through the recompression region as the edges of the SPs converge toward the reattachment point. Though the curves are within or close to the uncertainty of the PSP measurement, the trends do show that with increasing number of subdivisions, the recompression is amplified.

C. Fluctuating Pressure Measurements

High-frequency pressure measurements at two radial locations along the base for each of the four configurations were first time averaged and then compared to the current mean static-pressure tap measurements (Fig. 9) with good agreement. RMS pressure fluctuation levels normalized by the mean base pressure are shown in Fig. 12. These results show that the rms pressure fluctuations decreased with increasing cylinder divisions or by subdividing the recirculation region and eliminating the associated low-order azimuthal instability modes. Compared to the no-control case, the rms pressure fluctuations decreased approximately 21, 27, and 39% at the outer radial location ($r/R_0 = 0.84$) for the one-half-, one-third-, and one-fourth-cylinder SP cases, respectively, and 8, 26, and 36% for the inner radial location ($r/R_0 = 0.56$). A considerable decrease in the rms level occurs between the outer location compared to that of the inner location (14% for the no-control case and 32, 17, and 20% for the SP configurations). Again, the bars are representative of a plus or minus one standard deviation in the collected data. The rms pressure levels for the no-control case compare well with those reported by Janssen and Dutton [33] for the same radial locations, having values on the order of 5% of the mean base pressure and a similar decrease in rms fluctuations between locations. Janssen and Dutton used a similar 63.5 mm diameter blunt afterbody with a freestream Mach number of 2.46. RMS measurements of base pressure for transonic separated flows have also shown a decrease in level with increasing radius [31].

A comparison of the PSD estimates of the base pressure fluctuations for the no-control and various control cases is presented in Fig. 13. In this figure, $G_{pp}(f)$, the one-sided PSD as a function of frequency, is multiplied by the frequency and plotted on a semilog scale versus frequency. The PSD is plotted in this way so that the fluctuating energy content at the corresponding frequency is more clearly visible.

The PSDs for the two radial locations for the no-control case in Fig. 13a display qualitatively similar behavior. Both reveal gradual increases in the PSD estimates for increasing frequencies up to approximately 700 Hz. Upon passing 700 Hz, the PSD estimates experience a dramatic increase to nearly identical sharp peaks near 850 Hz (Strouhal number based on freestream velocity and base diameter, $St_D = 0.094$). After reaching the peak, the PSDs decline rapidly until about 1000 Hz. Past 1000 Hz, the PSDs exhibit little change in magnitude through 2000 Hz, at which point there is a steady decline through the remainder of frequencies. Despite being similar in shape, the PSDs for the two radial locations display significant differences in magnitude. The PSD for the outer location is discernibly smaller at all frequencies, which is consistent with the smaller rms values recorded at that location in Fig. 12. These PSD profiles replicate the data presented in [33] in general shape and the predominant peak locations for similar radial locations on the blunt afterbody.

The PSD estimates for the one-half-cylinder case, shown in Fig. 13b, again are comparable in form for the different radial locations. Both reveal a steady increase in magnitude with increasing frequency up to about 700 Hz, at which point the PSDs increase more noticeably to a broader peak, centered near 1000 Hz ($St_D = 0.11$). Beyond the maximum, the PSD at the outer location $r/R_0 = 0.84$ experiences a steady decrease through 3000 Hz, followed by a steeper trail off. For the inner location $r/R_0 = 0.56$, the PSD declines abruptly after the peak until roughly 1200 Hz ($St_D = 0.13$). Following 1200 Hz, the PSD decreases slightly until 3000 Hz, after which it declines more rapidly through the remainder of the measured frequencies. There is a more substantial magnitude difference in the PSDs between the two locations than for the

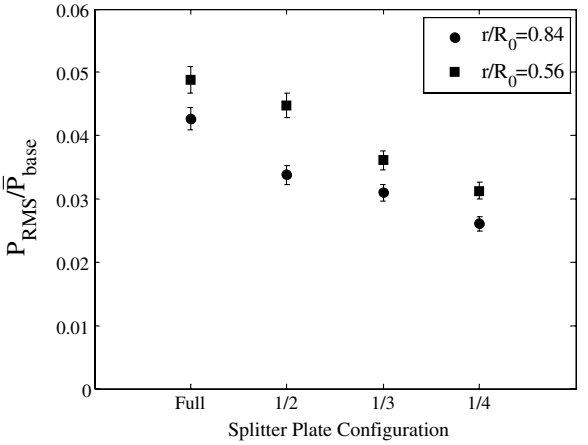

Fig. 12 Normalized rms pressure fluctuations for the splitter plate configurations.

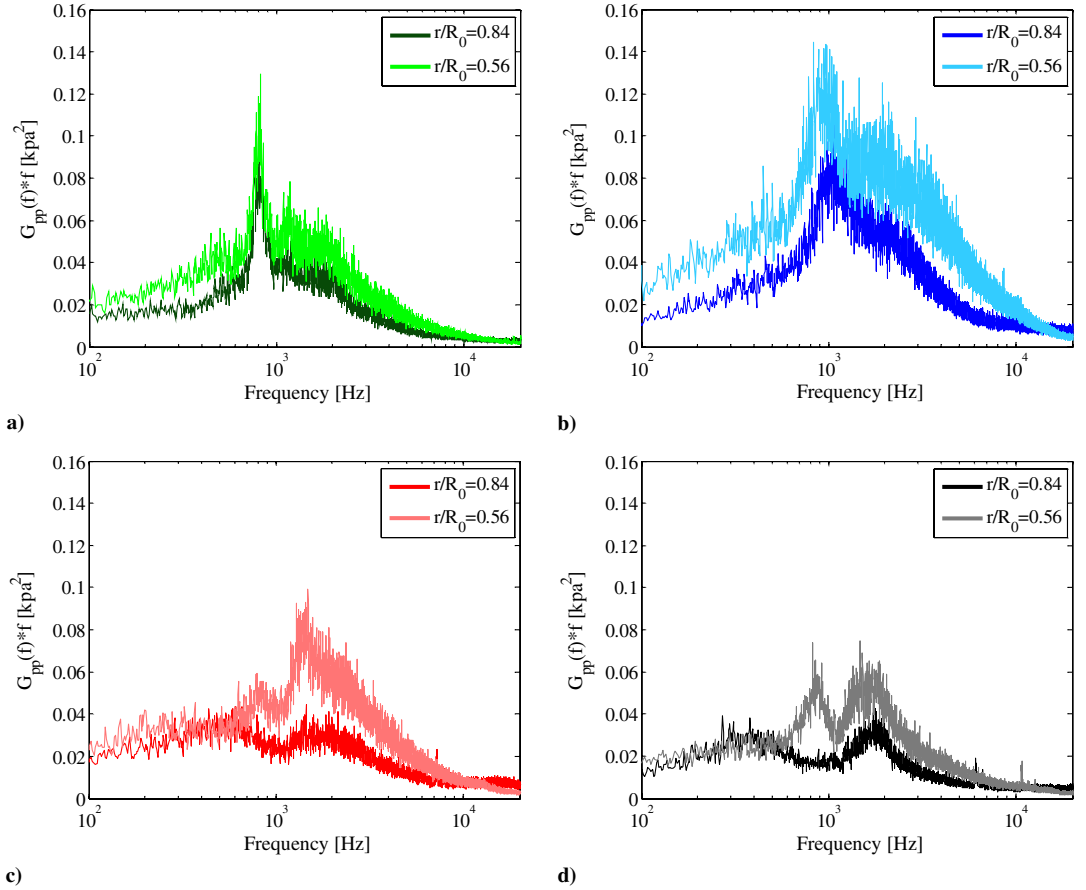

Fig. 13 One-sided PSD multiplied by frequency for a) no control, b) one-half-cylinder SP, c) one-third-cylinder SP, and d) one-fourth-cylinder SP.

no-control case, which again is consistent with the larger deviation in rms fluctuations seen in Fig. 12.

For the one-third-cylinder SP configuration, the PSDs (shown in Fig. 13c) for the two radial locations no longer display similar shapes; however, both exhibit a discernible bimodal distribution. The PSD at outer location $r/R_0 = 0.84$ experiences two relatively broad peaks, centered at frequencies about 600 Hz ($St_D = 0.067$) and 1800 Hz ($St_D = 0.20$). The PSD at inner location $r/R_0 = 0.56$ reveals a gradual increase to a first, smaller peak near 800 Hz ($St_D = 0.089$), a slight trough, then a substantial increase to the larger peak, centered at approximately 1400 Hz ($St_D = 0.16$). Beyond the large peak, the PSD declines steadily through the higher frequencies.

The PSDs for the one-fourth-cylinder SP configuration, shown in Fig. 13d, at both locations, exhibit a dominant bimodal distribution. The outer location shows two broad peaks centered at frequencies of about 400 Hz ($St_D = 0.044$) and 1800 Hz ($St_D = 0.20$). The two sharper peaks experienced by the inner transducer location are centered about 850 Hz ($St_D = 0.094$) and 1600 Hz ($St_D = 0.18$). Additionally, the lower-frequency peak at the inner location appears to be in antiphase with the PSD-estimated peaks experienced at the outer transducer.

A relatively broadband spectrum of energy (including the just described peaks) is present for the no-control, one-half-, one-third-, and one-fourth-cylinder SP configurations. Comparing the no-control case to the SP control cases, it is apparent that there is a further broadening or spreading of fluctuating energy across the spectrum of frequencies with increasing number of wake subdivisions. The single, distinct peak near 850 Hz in the no-control case has shifted to a fuller, rounder peak at increased frequencies for the one-half-cylinder case. Because the inner and outer radial locations experience similar fluctuating energy distributions, the dominant low-frequency pressure fluctuations are thought to be caused by a global pulsing phenomenon of the recirculation region. With the use of simultaneous transducer measurements (both radially and azimuthally separated transducers) and the finding of a zero time delay peak in the calculated cross correlations, Janssen and Dutton [33] hypothesized the same global mechanism affecting the base region for the flat base. The fluctuating energy decreases in magnitude and begins to disperse into two dominant modes for the one-third-cylinder case and, finally, into two comparable peaks for the one-fourth-cylinder case. The dissimilarity in fluctuating pressure distributions between the two radial locations observed for both the one-third- and one-fourth-cylinder cases could further suggest that the near-wake subdivisions altered the global instability mode within the recirculation region. Additionally, the prevailing bimodal distribution implies that multiple dominant mechanisms are present, contributing to the pressure fluctuations on the base.

The higher frequency peaks are thought to be associated with the global pulsing of the recirculation region. These peaks tend to increase in frequency with increasing number of cylinder divisions as the lower order azimuthal modes are eliminated. The shift in energy to the second mode, which was observed to be stronger at the inner radial location and more prevalent as the number of cylinder divisions increased, could be attributed to fluctuations from secondary recirculation regions that have formed, along the joints where the SPs meet the base, as mentioned previously. Secondary recirculation regions have been shown to be highly unsteady [29] and can be attributed to lower-frequency oscillations near the corner [30].

Pressure fluctuations, in both the normalized rms magnitudes in Fig. 12 and the PSD estimates in Fig. 13, are measured to be lower at the outer radial position compared to the inner position. The outer high-frequency transducer was located at a radial distance ($r/R_0 = 0.84$), which coincidentally was near the observed location of the separation ring from the flow visualizations. This location could be less susceptible to oscillations due to the impingement of pressure waves from the reversed flow on the solid base surface.

Additionally, with increasing number of SP divisions, the pressure fluctuation levels at both radial locations have been shown to decrease. Similar reductions in pressure fluctuations were noted by

Janssen and Dutton [34] when sub-boundary-layer strip tabs were implemented on a cylindrical afterbody, upstream of separation. These strip tabs were shown to dampen turbulent structures, stabilize motions in the shear layer and recirculation region, decrease mass entrainment, and consequently increase base pressure. By eliminating these presumed azimuthal modes in the current work, the SPs tended to stabilize the motion of the recirculation region but seem to have had little effect on shear layer growth (as seen in schlieren photographs) and thus mass entrainment. Therefore, despite lower base pressure rms values (compared to the no-control geometry), lower time-averaged base pressures were experienced with the SPs. From these observations, the shear layer turbulent structures and instability modes seem to be a better target for flow-control influence as opposed to those in the recirculation region.

V. Conclusions

Inserting triangular SPs into the recirculation region behind a blunt-based axisymmetric body in supersonic flow divided the large-scale recirculation region and eliminated the low-order azimuthal instability modes within the recirculation region. Time-averaged and high-frequency static-pressure measurements, schlieren imaging, surface flow visualization, and PSP measurements were conducted to give insight into the fluid dynamic mechanisms that govern these high-speed separated flows and to determine the flow-control authority of these passive devices. The conclusions from these experiments are as follows:

1) Insertion of the solid plates into the separated region affected the near-wake flow structure such that the time-averaged radial base pressure distribution was altered. The area-integrated mean pressure acting on the base was observed to increase slightly by the SP additions and thus did not lead to a reduction in drag. This result is not consistent with the findings of the numerical simulations conducted by Sandberg and Fasel [24] for reduced circumferential domains sizes at reduced Reynolds numbers. Key differences between the computations and experiments potentially contributing to the differing results were addressed.

2) Schlieren images show that the SP presence caused little change in the large-scale behavior of the near wake, outside of the recirculation region.

3) Normalized rms pressure levels were substantially decreased with increasing number of near-wake divisions. For all configurations, the normalized rms magnitudes of the inner radial location were observed to be higher than for the outer location.

4) The PSD estimates illustrate the differences in base pressure fluctuations at two radial locations for the no-control and SP cases. Compared to the inner radial location, the outer location, in general, shows lower PSD values for all frequencies. For the no-control configuration, a sharp peak near 850 Hz was observed and is attributed to global pulsing of the recirculation region. For the one-half-cylinder SP configuration, the fluctuating pressure peak is broadened to higher frequencies. For the one-third- and one-fourth-cylinder SP configurations, two distinct peaks in the PSDs were observed, implying that more than one mechanism is accountable for the pressure fluctuations on the base. The additional lower-frequency mode is thought to be caused by smaller, secondary recirculation regions that were observed in the corners where the SPs join with the base. These corner interactions were apparent in the two innermost static-pressure measurements on the base, the flow visualization images, and the PSP results and, in general, seemed to increase in magnitude with increasing number of wake subdivisions.

5) The recirculation region may not be the most sensitive location to apply flow control. Rather, the shear layer that develops from the separation point may be a more influential site for implementing flow-control methodologies.

Acknowledgments

The authors would like to thank the Army Research Office with Frederick Ferguson as program monitor (grant number W911NF-08-1-0434) for supporting this research. Any opinions, findings and conclusions, or recommendations expressed in this material are those of the authors and do not necessarily reflect the views of Army Research Office. Additionally, we would like to thank our colleagues, Brad DeBlauw and Thomas Herges, for their discussion, input, and assistance regarding this work.

References

[1] Rollstin, L. R., "Measurement of In-Flight Base Pressure on an Artillery-Fired Projectile," *Journal of Spacecraft and Rockets*, Vol. 27, No. 1, 1990, pp. 5–6. doi:10.2514/3.26096

[2] Herrin, J. L., and Dutton, J. C., "Supersonic Base Flow Experiments in the Near Wake of a Cylindrical Afterbody," *AIAA Journal*, Vol. 32, No. 1, 1994, pp. 77–83. doi:10.2514/3.11953

[3] Papamoschou, D., and Roshko, A., "Compressible Turbulent Shear Layer: An Experimental Study," *Journal of Fluid Mechanics*, Vol. 197, 1988, pp. 453–477. doi:10.1017/S0022112088003325

[4] Chapman, D. R., "An Analysis of Base Pressure at Supersonic Velocities and Comparison with Experiment," NACA TN-2137, 1950.

[5] Korst, H. H., "A Theory for Base Pressures in Transonic and Supersonic Flows," *Journal of Applied Mechanics*, Vol. 23, No. 4, 1956, pp. 593–600.

[6] Bourdon, C. J., and Dutton, J. C., "Planar Visualizations of Large-Scale Turbulent Structures in Axisymmetric Supersonic Separated Flows," *Physics of Fluids*, Vol. 11, No. 1, 1999, pp. 201–213. doi:10.1063/1.869913

[7] Bourdon, C. J., and Dutton, J. C., "Shear Layer Flapping and Interface Convolution in a Separated Supersonic Flow," *AIAA Journal*, Vol. 38, No. 10, 2000, pp. 1907–1915. doi:10.2514/2.844

[8] Sahu, J., "Three Dimensional Base Flow Calculation for a Projectile at Transonic Velocity," AIAA Paper 1986-1051, 1986.

[9] Sahu, J., "Supersonic Flow Over Cylindrical Afterbodies with Base Bleed," *Computational Mechanics*, Vol. 2, No. 3, 1987, pp. 176–184. doi:10.1007/BF00571023

[10] Chuang, C. C., and Chieng, C. C., "Supersonic Base-Flow Computation Using Higher-Order Closure Turbulence Models," *Journal of Spacecraft and Rockets*, Vol. 33, No. 3, 1996, pp. 374–380. doi:10.2514/3.26770

[11] Fureby, C., Nilsson, Y., and Andersson, K., "Large Eddy Simulation of Supersonic Base Flow," AIAA Paper 1999-0426, 1999.

[12] Forsythe, J. R., Hoffmann, K. A., Cummings, R. M., and Squires, K. D., "Detached-Eddy Simulation with Compressibility Corrections Applied to a Supersonic Axisymmetric Base Flow," *Journal of Fluids Engineering*, Vol. 124, No. 4, 2002, pp. 911–923. doi:10.1115/1.1517572

[13] Kawai, S., and Fujii, K., "Computational Study of Supersonic Base Flow Using Hybrid Turbulence Methodology," *AIAA Journal*, Vol. 43, No. 6, 2005, pp. 1265–1275. doi:10.2514/1.13690

[14] Simon, F., Deck, S., Guillen, P., Sagaut, P., and Merlen, A., "Numerical Simulation of the Compressible Mixing Layer Past an Axisymmetric Trailing Edge," *Journal of Fluid Mechanics*, Vol. 591, 2007, pp. 215–253. doi:10.1017/S0022112007008129

[15] Sivasubramanian, J., Sandberg, R. D., Von Terzi, D. A., and Fasel, H. F., "Numerical Investigation of Transitional Supersonic Base Flows with Flow Control," *Journal of Spacecraft and Rockets*, Vol. 44, No. 5, 2007, pp. 1021–1028. doi:10.2514/1.28673

[16] Weiss, P. E., and Deck, S., "Control of the Antisymmetric Mode ($m = 1$) for High Reynolds Axisymmetric Turbulent Separating/Reattaching Flows," *Physics of Fluids*, Vol. 23, No. 9, 2011, Paper 095102. doi:10.1063/1.3614481

[17] Stanewsky, E., "Adaptive Wing and Flow Control Technology," *Progress in Aerospace Sciences*, Vol. 37, No. 7, 2001, pp. 583–667. doi:10.1016/S0376-0421(01)00017-3

[18] Crittenden, T. M., and Glezer, A., "A High-Speed, Compressible Synthetic Jet," *Physics of Fluids*, Vol. 18, 2006, Paper 017107. doi:10.1063/1.2166451

[19] Shang, J. S., Surzhikov, S. T., Kimmel, R., Gaitonde, D., Menart, J., and Hayes, J., "Mechanisms of Plasma Actuators for Hypersonic Flow Control," *Progress in Aerospace Sciences*, Vol. 41, No. 8, 2005, pp. 642–668.

doi:10.1016/j.paerosci.2005.11.001
[20] Herrin, J. L., and Dutton, J. C., "Effect of a Rapid Expansion on the Development of Compressible Free Shear Layers," *Physics of Fluids*, Vol. 7, No. 1, 1995, pp. 159–171. doi:10.1063/1.868737
[21] Addy, A. L., and White, R. A., "Optimization of Drag Minimums Including Effects of Flow Separation," *Transactions of the ASME: Journal of Engineering Industry*, Vol. 95, Series B, No. 1, 1973, pp. 360–364. doi:10.1115/1.3438136
[22] Mathur, T., and Dutton, J. C., "Velocity and Turbulence Measurements in a Supersonic Base Flow with Mass Bleed," *AIAA Journal*, Vol. 34, No. 6, 1996, pp. 1153–1159. doi:10.2514/3.13206
[23] Sandberg, R. D., and Fasel, H. F., "Numerical Investigation of Transitional Supersonic Axisymmetric Wakes," *Journal of Fluid Mechanics*, Vol. 563, 2006, pp. 1–41. doi:10.1017/S0022112006000899
[24] Sandberg, R. D., and Fasel, H. F., "Direct Numerical Simulations of Transitional Supersonic Base Flows," *AIAA Journal*, Vol. 44, No. 4, 2006, pp. 848–858. doi:10.2514/1.18177
[25] Sandberg, R. D., "Numerical Investigation of Transitional and Turbulent Supersonic Axisymmetric Wakes," Ph.D. Dissertation, Department of Aerospace and Mechanical Engineering, Univ. of Arizona, Tucson, AZ, 2004.
[26] Mabey, D. G., "Analysis and Correlation of Data on Pressure Fluctuations in Separated Flow," *Journal of Aircraft*, Vol. 9, No. 9, 1972, pp. 642–645. doi:10.2514/3.59053
[27] Corcos, G. M., "Resolution of Pressure in Turbulence," *Journal of the Acoustical Society of America*, Vol. 35, No. 2, 1963, pp. 192–199. doi:10.1121/1.1918431
[28] Hall, S. D., Behnia, M., Fletcher, C. A. J., and Morrison, G., "Investigation of the Secondary Corner Vortex in a Benchmark Turbulent Backward-Facing Step Using Cross-Correlation Particle Imaging Velocimetry," *Experiments in Fluids*, Vol. 35, No. 2, 2003, pp. 139–151. doi:10.1007/s00348-003-0626-9
[29] Spazzini, P. G., Iuso, G., Onorato, M., Zurlo, N., and DiCicca, G. M., "Unsteady Behavior of Back-Facing Step Flow," *Experiments in Fluids*, Vol. 30, No. 5, 2001, pp. 551–561. doi:10.1007/s003480000234
[30] Deck, S., and Thorigny, P., "Unsteadiness of an Axisymmetric Separating-Reattaching Flow: Numerical Investigation," *Physics of Fluids*, Vol. 19, No. 6, 2007, Paper 065103. doi:10.1063/1.2734996
[31] Depres, D., Reijasse, P., and Dussauge, J. P., "Analysis of Unsteadiness in Afterbody Transonic Flows," *AIAA Journal*, Vol. 42, No. 12, 2004, pp. 2541–2550. doi:10.2514/1.7000
[32] Amatucci, V. A., Dutton, J. C., Kuntz, D. W., and Addy, A. L., "Two-Stream, Supersonic, Wake Flowfield Behind a Thick Base, Part I. General Features," *AIAA Journal*, Vol. 30, No. 8, 1992, pp. 2039–2046. doi:10.2514/3.11177
[33] Janssen, J. R., and Dutton, J. C., "Time-Series Analysis of Supersonic Base-Pressure Fluctuations," *AIAA Journal*, Vol. 42, No. 3, 2004, pp. 605–613. doi:10.2514/1.4071
[34] Janssen, J. R., and Dutton, J. C., "Sub-Boundary-Layer Disturbance Effects on Supersonic Base-Pressure Fluctuations," *Journal of Spacecraft and Rockets*, Vol. 42, No. 6, 2005, pp. 1017–1024. doi:10.2514/1.12769

J. Sahu
Associate Editor